frontiers | Frontiers in Astronomy and Space Sciences

TYPE Original Research
PUBLISHED 01 November 2024
DOI 10.3389/fspas.2024.1465230

OPEN ACCESS

EDITED BY
David Hysell,
Cornell University, United States

REVIEWED BY
Yun Gong,
Wuhan University, China
Yen-Jung Wu,
University of California, Berkeley,
United States

*CORRESPONDENCE
Katrina Bossert,
katrina.bossert@asu.edu

RECEIVED 15 July 2024
ACCEPTED 02 September 2024
PUBLISHED 01 November 2024

CITATION
Bossert K, Kumari K, Inchin P, Norrell J, Eckermann S, Pautet P-D, Martinis C, Kjellstrand CB, Phillips S, Snively J, Zhao Y and Zettergren M (2024) Influences of the quasi-two-day wave on plasma bubble behavior over south America.
Front. Astron. Space Sci. 11:1465230.
doi: 10.3389/fspas.2024.1465230

Influences of the quasi-two-day wave on plasma bubble behavior over south America

Katrina Bossert[1,2]*, Komal Kumari[3], Pavel Inchin[4], Jessica Norrell[1], Stephen Eckermann[5], Pierre-Dominique Pautet[6], Carlos Martinis[7], Carl Bjorn Kjellstrand[1], Sophie Phillips[1], Jonathan Snively[8], Yucheng Zhao[6] and Matthew Zettergren[8]

[1]School of Earth and Space Exploration, Arizona State University, Tempe, AZ, United States, [2]School of Mathematical and Statistical Sciences, Arizona State University, Tempe, AZ, United States, [3]High Altitude Observatory, National Center for Atmospheric Research, Boulder, CO, United States, [4]Computational Physics, Inc., Springfield, VA, United States, [5]U.S. Naval Research Laboratory, Washington, DC, United States, [6]Center for Atmospheric and Space Sciences, Utah State University, Logan, UT, United States, [7]Center for Space Physics, Astronomy Department, Boston University, Boston, MA, United States, [8]Physical Sciences Department, Embry-Riddle Aeronautical University, Daytona Beach, FL, United States

Equatorial Plasma Bubbles (EPBs) are a region of depleted ionospheric densities. EPBs are known to fluctuate both seasonally and day to day, and have been linked to changes in solar activity, geomagnetic activity, and seeding resulting from dynamics occurring at lower altitudes. Here, EPB activity is investigated over a 15-day period with overlapping coincident ground-based 630 nm oxygen airglow measurements, near-infrared hydroxyl mesospheric temperature mapper (MTM) measurements, and Rate Of change of Total Electron Content Index (ROTI) values. The data are compared with the Navy Global Environmental Model (NAVGEM) reanalysis over the same time period. It is found that several days with strong EPB activity coincided with the positive/northward meridional wind phase of the quasi-two-day wave (QTDW) in the mesosphere. These initial observations indicate correlations of the QTDW phase and the occurrence rates of EPBs, and suggest a need for further investigations to assess potential causal relationships that may affect the variability and prevalence of EPBs.

KEYWORDS

equatorial plasma bubbles, quasi-two-day-wave, roti, gravity waves (GWs), airglow

1 Introduction

Equatorial plasma bubbles (EPBs) can have significant implications for the state of the ionosphere as well as ionospheric radio remote sensing and communications (Hysell, 2000; Sousasantos et al., 2023). While there have been advances over the years in understanding EPBs, there are still outstanding issues towards understanding both their smaller-scale mechanisms, global scale modeling, and forecasting (Huba, 2022). EPBs have been known to vary from day to day (Aa, et al., 2023a), seasonally (Chou et al., 2020; Stolle, et al., 2006), and with differing geomagnetic activity (Martinis et al., 2005; Abdu, 2012; Carmo et al., 2023; Amadi et al., 2023). EPB formation occurs most prominently during the hours after sunset, when a steep gradient in electron density forms contributing to the growth rate of

the Rayleigh-Taylor (R-T) instability (Sultan, 1996; Huang and Hairston, 2015; Hudson and Kennel, 1975), ultimately leading to equatorial spread F (ESF). While the generation of ESF is linked to this post-sunset time period, the R-T instability is further triggered by meridional wind gradients in the F-region, which can change due to a number of factors (Huba and Krall, 2013). These driving factors that cause EPB seeding include geomagnetic and solar activity (Adhya and Valladares, 2023; Sori et al., 2021; Kepkar et al., 2020) and gravity wave (GW) propagation into the thermosphere and ionosphere (Yokoyama et al., 2019; Chou et al., 2023; Saha et al., 2022; Takahashi et al., 2009; Fritts et al., 2008; Singh et al., 1997).

Observations of EPBs and ESF have been made over many decades via multiple measurement techniques (e.g., Bhattacharyya, 2022, and references therein). Recently, ICON and GOLD satellite missions have provided insight into EPB variability and generation (Huba et al., 2021; Karan et al., 2020; Karan et al., 2023; Aa et al., 2023b; Park et al., 2022). However, EPBs have also been studied with numerous ground-based instruments (Aa et al., 2019; Haase et al., 2010; Hysell and Burcham, 1998). The research presented here uses Rate Of change of Total electron content Index (ROTI) and 630.0 nm oxygen airglow from an all-sky imager to classify the presence and extent of EPBs. Airglow imaging provides spatial observations allowing for the 2D study of EPB formation and evolution (Pautet et al., 2009; Martinis et al., 2009). ROTI has been used in numerous studies of ESF and EPBs, due to its correlation with larger-scale plasma irregularities that are associated with ESF and airglow depletions (Carmo et al., 2023; Lay, 2018; de Jesus et al., 2020; Rajesh et al., 2022).

The Quasi-Two-Day Wave (QTDW) is a large-scale wave that is often observed to be westward propagating with a zonal wavenumber of 3 (Ern et al., 2013; Burks and Leovy, 1986; Lieberman et al., 2017). The QTDW is caused by the instability of the summer hemisphere easterly jet, which results in an amplitude that is most notable in meridional winds in the mesosphere and lower thermosphere (MLT) region (Singh et al., 2024). It is typically observed in the summertime hemisphere, and has been well studied through multiple observations (He et al., 2021; Craig et al., 1980; Pancheva et al., 2018; Iimura et al., 2021; Walterscheid et al., 2015; Hecht et al., 2010). The QTDW has been shown to modulate the ionospheric dynamo and electron density (Yue et al., 2012; Pancheva et al., 2006; Forbes et al., 2021). Studies also have demonstrated the implications and interactions of the QTDW with GW dissipation, generation, and filtering (Ern et al., 2013; Yasui et al., 2021; Jacobi and Pogoreltsev, 2006). These findings underscore the multiple possible pathways through which the QTDW may influence the lower thermosphere and ionosphere. In the observations presented in this case study, relationships between EPB appearance and extent are compared with QTDW phase within the MLT region using ROTI, hydroxyl mesospheric temperature mapper (MTM) measurements, and 630 nm airglow images, in conjunction with the Navy Global Environmental Model (NAVGEM) output. Additionally, these observations are compared with GW activity in the stratosphere and mesosphere as measured by the MTM, the Atmospheric InfraRed Sounder (AIRS) and NAVGEM. These are reported and discussed in the subsequent Sections 2, 3.

2 Materials and methods

Observations from multiple instruments were used from the period over 10–24 January 2015. These measurements demonstrate fluctuations in ROTI and airglow associated with plasma bubbles. The ionosphere-thermosphere measurements are combined with hydroxyl MTM measurements in conjunction with NAVGEM reanalysis data for comparison of coincident dynamics in the MLT region.

2.1 ROTI observations over south America

The ionospheric irregularities are based on the ROTI (Pi et al., 1997), which represents a standard derivation of the rate of change of TEC (ROT):

$$ROTI = \sqrt{\langle ROT^2 \rangle - \langle ROT \rangle^2} \tag{1}$$

where

$$ROT = \frac{TEC_t - TEC_{t-\delta t}}{\delta t} \tag{2}$$

Here, TEC is calculated based on 30 s phase observations at GPS L1 and L2 frequencies for each satellite-station pair (Inchin et al., 2023). For this case study, 88 stations extending throughout Chile are used. The time window of 5 min is chosen to calculate a variance in Equation 1, using the ROT calculated in Equation 2. The ROTI values are calculated using GPS receiver sites in South America using a 40-degree elevation cut off. Figure 1A shows all data points included south of geographic latitude 15S. Figure 1B shows data points of ROTI for geographic latitudes south of 30S. This plot highlights ionosphere fluctuations occurring at more southern latitudes and furthermore demonstrates a periodic nature to these southern increased ROTI values. To highlight regions of increased ROTI, Figure 1C shows the average ROTI value of datapoints binned in a 1-h period. Most peaks in ROTI occur between 1-3UT, which corresponds to post-sunset local times as is expected for the onset of EPB (Sultan, 1996; Huang, 2018; Panda et al., 2019). However, there are exceptions to post-sunset formation, and spikes in ROTI are observed after midnight LT in some instances. During the observation period, this was the case on 23 January. These post-midnight EPBs may be generated by a different mechanism, but are still frequently observed (Martinis et al., 2005; Otsuka, 2018; Yizengaw et al., 2013). In the observations presented, the largest post-sunset ROTI values were observed on 16, 18, 20, and 24 January, with mean values at these times ranging from 0.1 to 0.18 TECu/min. The lowest ROTI values were on 13 and 15 January, with mean values of measured ROTI post-sunset around or less than 0.03 TECu/min.

2.2 Optical ground-based observations

Airglow emissions in the thermosphere at 630 nm have previously been used to study depletions associated with EPBs near 250 km in altitude (Martinis et al., 2018; Hickey and Martinis, 2018). Data from an imager at the El Leoncito observatory (31.8S, 69.4W) that belongs to the Boston University network of all-sky

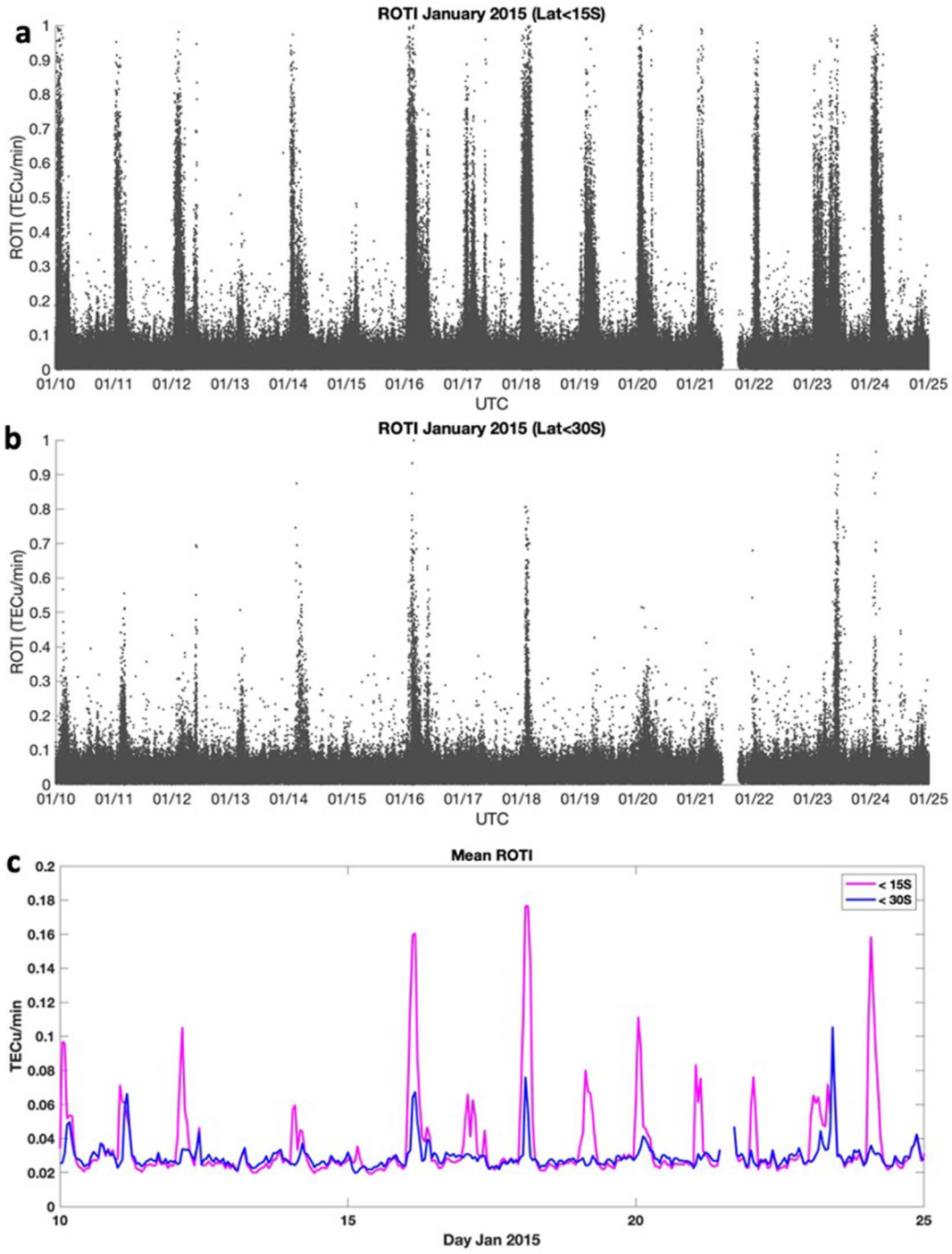

FIGURE 1
Plot **(A)** shows the ROTI values at all geographic locations south geographic latitude 15S. Plot **(B)** is the same as plot **(A)** but for locations south of 30S. Plot **(C)** shows the average of ROTI values binned into 1 h time intervals for locations south of 15S (pink) and 30S (blue).

imagers (Martinis et al., 2018) were used to classify the presence of ESF associated depletions in 630 nm airglow from 10–24 January. Each hour was classified with an activity level as either (1) a depletion extending to magnetic latitude 20S or further, (0.5) north of magnetic latitude 20S, (−1) clear with no visible depletions, or (0) no data available. Figure 2A summarizes these observations. From January 16–24, depletions were observed on all nights. The nights of January 16, 18, and 24 demonstrate depletions extending farthest southward beyond −20 MLAT. Examples of significant depletions are shown in Figures 2D, E for January 16 and 18 respectively. To determine conditions that may contribute to differing EPB on each day, geomagnetic and solar conditions were compared to the observations. The SuperMAG Auroral Electrojet (SME) index (Gjerloev, 2012; Newell and Gjerloev, 2011a; 2011b) is indicative of

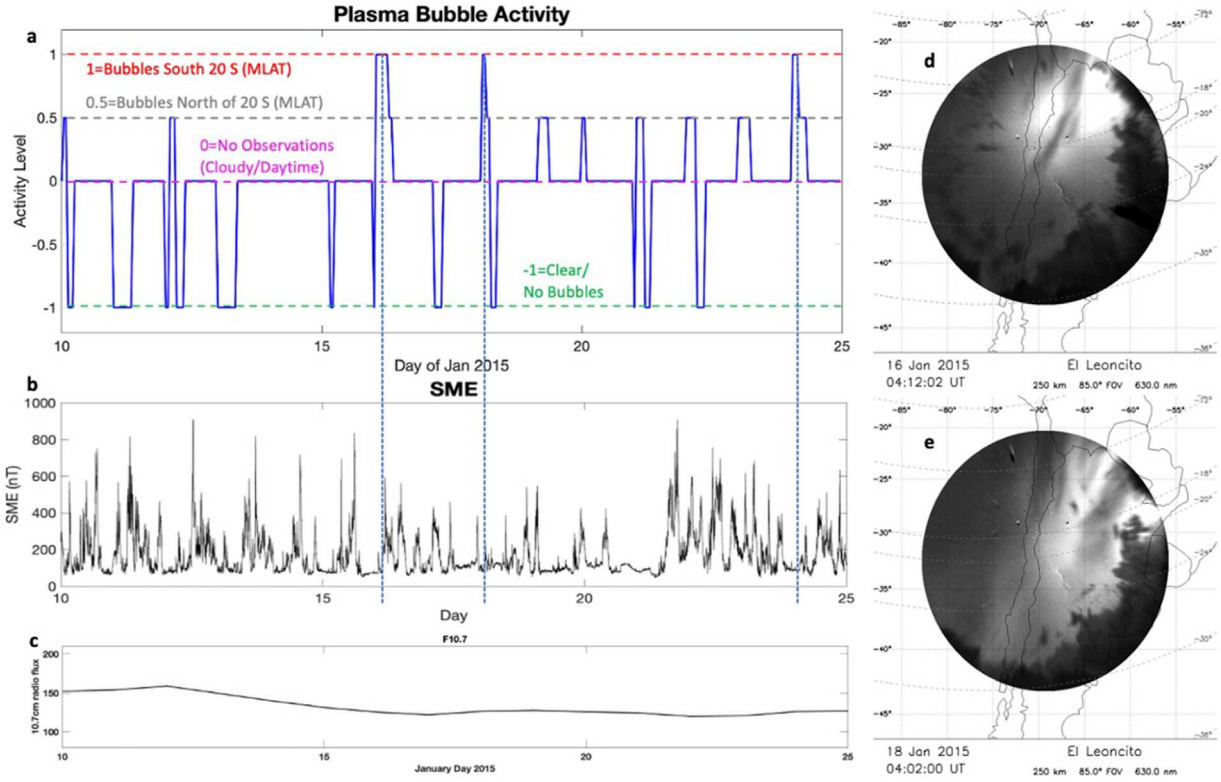

FIGURE 2
Plot **(A)** shows depletions observed in the 630 nm airglow with a value of one corresponding to depletions extending further south than −20 MLAT, a value of 0.5 corresponding to depletions north of −20 MLAT, a value of −1 indicating data but no observed depletions, and a value of 0 indicating no data. Plot **(B)** shows the SME index indicating the level of auroral activity. Plot **(C)** shows the F10.7 value indicating solar activity. Plots **(D)** and **(E)** show significant depletions in the 630 nm airglow on 16 and 18 January 2015.

global auroral power and indicates times of increased geomagnetic activity. This dataset is plotted in Figure 2B, and while fluctuations exist, there are no notable differences between days of significant depletions versus no depletions. Additionally, solar activity is denoted with the F10.7 index and plotted in Figure 2C. These values show little variation over the period of observations, indicating that the fluctuations in EPB activity were not necessarily related to solar activity in this case.

The MTM located at the nearby Andes Lidar Observatory (ALO) (30.3S, 70.7W) measures temperatures from hydroxyl (OH) airglow near 87 km in altitude (PugmireJonathan Rich, 2018). These measurements provide information regarding middle atmospheric dynamics with regards to both larger-scale temperature averages, and GW activity down to horizontal wavelengths of 10 km. Figure 3A shows nightly temperature averages from the MTM using 5 × 5 zenith pixel averages from each image over the period of observations, where an apparent 2-day fluctuation in temperatures from warm to cooler values is observed. A previous comparison of the MTM OH rotational temperatures (OH T) with other well-calibrated instruments (an FTIR spectrometer and sodium lidar) has shown that nightly mean temperatures, referenced to the 87 km lidar mean temperatures, are accurate to about +/−5K (Pendleton et al., 2000; Zhao et al., 2005). Further details of the MTM data reduction and analysis are given in Taylor et al. (1999; 2001). In the study presented here, the nightly averages show differences of 20–30K between consecutive nights from 15–24 January 2015. Warmer values are observed on and before January 15, and on January 17, 19, 21, and 23. Cooler values are observed on January 16, 18, 20, 22, and 24. These fluctuations in temperature indicate the presence of a QTDW. The three largest histogram ROTI values are indicated on nights with red dots. The pink dot indicates the fourth largest histogram ROTI value, which corresponds to an EPB that was not observed south of −20 MLAT. These four nights coincide with the coldest average nightly temperatures measured by the MTM, and suggest a potential correlation in EPB activity with the colder MLT temperatures.

The nightly standard deviation (stdev) for each night of OH T measurements from the MTM is plotted in Figure 3B. This metric provides insight into GW activity present on a given night. A higher stdev indicates more wave activity. Figure 3C shows a zonal keogram (one line of data taken from the center of the MTM field of view along the zonal direction plotted for each mapper image over time) on a lower stdev night, and Figure 3D shows a zonal keogram on a more active night, with waves present that have periods ranging from several minutes to hours. The largest temperature perturbation on this day appears to be associated with dynamical changes occurring on the time scale of several hours, indicating a gravity wave that is likely much larger (100 s km to >1,000 km) than the field of view of the MTM. On 22 January, a minimum in temperature was observed. However, EPBs did not extend beyond −20MLAT and ROTI values

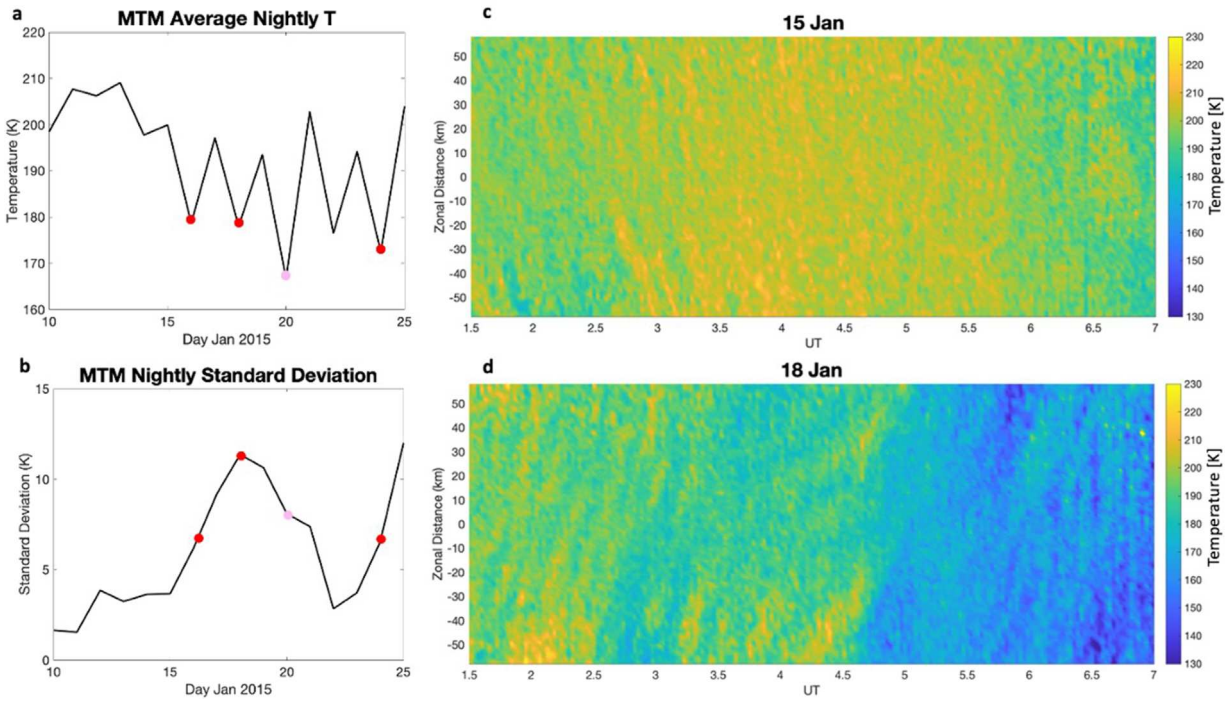

FIGURE 3
Plot **(A)** data show the nightly average OH temperatures plotted from the MTM. A 2-day fluctuation is apparent in the data from 15–24 January, with the three nights of largest ROTI values and 630 nm depletions extending below 20S MLAT denoted with red dots, and the fourth largest night of ROTI values is denoted in pink. These significant nights of EPB activity fall on the nights of coldest average temperatures. Plot **(B)** shows the nightly stdev of temperatures, a metric that denotes GW activity. Plots **(C)** and **(D)** show zonal keograms of MTM data for lower stdev (15 January) and higher stdev (18 January) nights, allowing for both long period and short period temperature fluctuations associated with GWs to be observed, especially on the more active night in **(D)**.

were similar to warm phase nights. On this particular night, a lower OH T stdev was measured, indicating lower GW activity over the field of view of the MTM.

3 Results

3.1 QTDW influences

Concurrent dynamics in the mesosphere were further investigated using NAVGEM reanalysis (Eckermann et al., 2018) that is extended above 100 km via hydrostatic blending with HWM winds and MSIS temperature and composition (Inchin et al., 2023). We note here that the NAVGEM reanalysis only contains observations up to 100 km and hydrostatically relaxes to MSIS and HWM climatology above this altitude. Thus, large scale influences associated with the QTDW are not reflected above 100 km. Figures 4A, B show global meridional (V), and zonal (U), winds plotted at 85 km in altitude for 18 January 2015, a day with significant ROTI values and 630 nm airglow depletions. The QTDW is primarily manifested in meridional winds, has zonal wavenumber of 3, and maximizes near 85 km in altitude, which is illustrated in Figure 4A. The QTDW is not readily apparent in zonal winds shown in Figure 4B, though may still have associated zonal wind amplitude. The phase over South America at the beginning of 18 January is mainly aligned with positive/northward meridional wind. The QTDW is present from the equatorial region to near 60S. Figures 4C, D show NAVGEM meridional and zonal winds averaged from 70-45W and 10-30S. Figure 4E shows the fit to zonal wavenumber three in meridional winds, demonstrating a strong presence of the QTDW, which increases in amplitude in the second half of the study period from ~50 m/s to ~80 m/s. Figure 4F shows the frequency-wavenumber spectrum verifying the presence of the QTDW. Figure 5 shows the ROTI data from Figure 1C overplotted with meridional winds from Figure 4C to demonstrate overlap of EPBs with the QTDW. The ROTI values show the strongest peaks aligning with the diurnal tidal winds near 200 km, expected for post sunset EPBs. Most notably, the strongest peaks occurred when the meridional winds associated with the QTDW are at a positive/northward peak near 85 km. This MLT trend is not observed in zonal winds, which do not have a strong QTDW signature (Figure 4D).

While post-sunset spikes in the ROTI and depletions in the 630 nm airglow are present on most days, the largest occurrences (highest ROTI, furthest southward depletions) coincide with the positive meridional winds associated with the QTDW in the mesosphere. Additionally, these stronger instances did not show a correlation with the solar or geomagnetic activity over the 2-week case study period. This suggests there may be a lower atmospheric influence associated with stronger EPBs linked to the meridional wind in the mesosphere. The MTM demonstrated that these increased times of EBPs corresponded both to colder

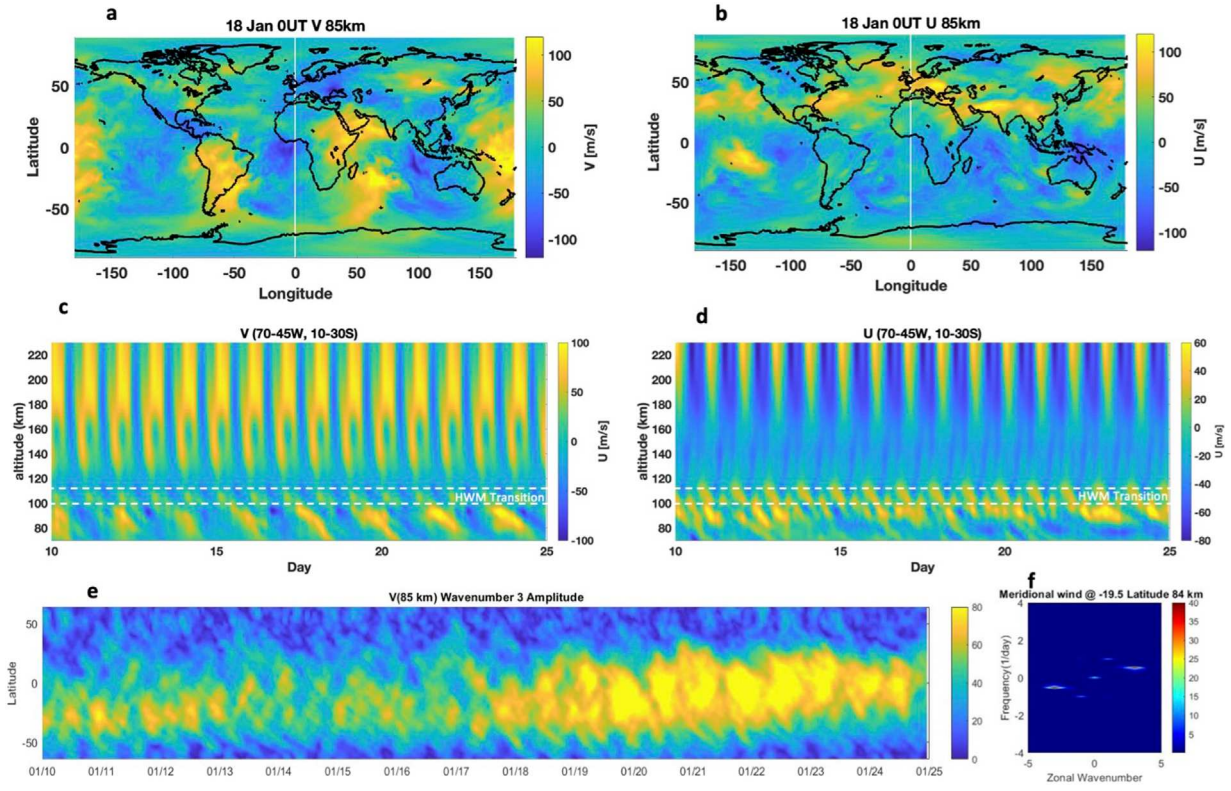

FIGURE 4
Plots **(A)** and **(B)** show NAVGEM meridional and zonal winds on 18 January 2015 at 0UT. The meridional wind clearly shows the QTDW signature (zonal wavenumber 3) in the southern hemisphere. Plots **(C)** and **(D)** show the NAVGEM meridional and zonal winds averaged from 45 to 70W and 10 to 30S, and plotted over altitude and time, which demonstrate a 2-day wave period in the meridional winds. Plot **(E)** shows the zonal wavenumber three fit of meridional winds over the 15 day period. Plot **(F)** shows a frequency-wavenumber plot demonstrating the presence of a QTDW.

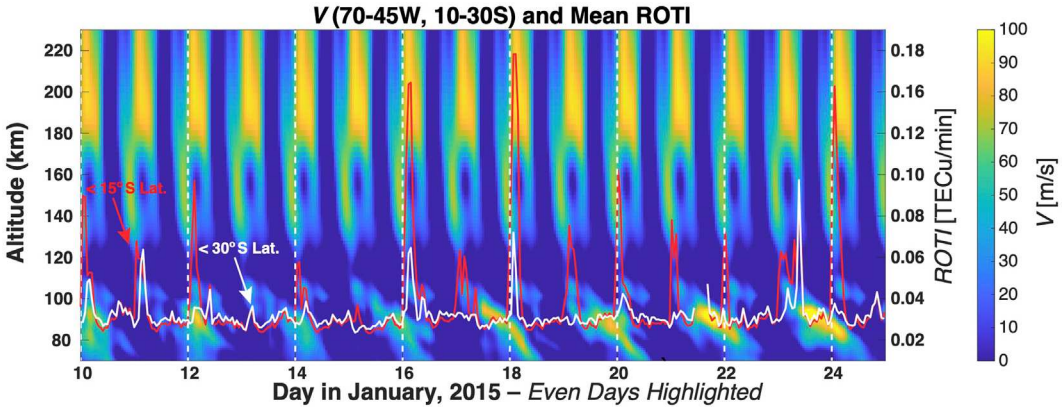

FIGURE 5
NAVGEM meridional winds averaged from 45 to 70W and 10 to 30S, and plotted over altitude and time overlapped with ROTI histograms from Figure 1C. The strongest ROTI values overlap with times where winds near 85–90 km are most strongly positive.

temperatures in the mesosphere and increased GW activity associated with higher stdev in the temperature measurements. These stronger events occurred starting January 16 and were not observed between January 10–15. Additionally, two nights where no peaks in ROTI were present, and no depletions were observed in the 630 nm airglow (13 and 15 January) corresponded to lower MTM OH T standard deviation (lower GW activity), higher MTM OH T, and southward meridional wind near 85 km associated with the QTDW during times of lower QTDW global amplitudes.

The coincidence of increased EPB activity during times of increased GW activity in the mesosphere and northward winds in the mesosphere implies that some aspects of lower atmosphere dynamics may influence the presence of EPBs. This has been well established, for instance, with studies of GW seeding of EPBs (Yokoyama et al., 2019; Taori et al., 2011; Fritts et al., 2008). Additionally, the influence of the QTDW on the ionosphere has been previously demonstrated (e.g., Yue et al., 2012). The observations presented here suggest that the QTDW itself may play a role in EPB generation, and/or provides a mechanism or environment for increased GW activity in a manner that may contribute to EPB seeding.

3.2 GW and interhemispheric influences

The MTM provides OH T data, from which stdev can be calculated. The OH T stdev indicates wave activity in a manner that can be compared over the 2-week period of study. The strongest wave activity observed in the MTM occurred also on days that overlapped with the coldest temperatures, and also coincided with the strongest EPB events and ROTI values observed over the study period. However, the MTM instrument itself is south of the magnetic equator, and it is expected that EPB seeding occurs closer to the equator. To gain more insight into links between variability in the lower atmosphere and ROTI/depletions in the ionosphere/thermosphere, the AIRS instrument onboard the NASA Aqua Satellite was used to determine brightness temperature perturbation variances in the stratosphere near 40 km in altitude, and is sensitive to GWs with vertical wavelengths of >10 km (Hoffmann and Alexander, 2009). The variances are associated with GW activity and were taken over regions in the northern hemisphere near the polar vortex and over the southern hemisphere region near ALO and coincident convection, both of which are potential sources of GWs that can influence the thermosphere. Additionally, AIRS brightness temperature perturbation variances near the equator were also included. Figure 6A shows the MTM standard deviation values to highlight days with higher GW activity in the MLT for comparison to AIRS data, and Figure 6B shows the resulting AIRS brightness temperature variances over the period from 10–24 January 2015. AIRS temperature perturbation variances in the northern hemisphere overlapping the polar vortex (40–60N) demonstrate an increase in GW activity that agrees with the MTM data from near 87 km and 30 S, and both measurements demonstrate a peak in activity near 18 January. There were no notable changes in AIRS brightness temperature variances near the equator. Some variability was observed in the southern hemisphere region (20-40 S) during this time period.

The standard deviation of temperatures was used from NAVGEM over several regions during the same time period to compare to the MTM and AIRS measurements. To obtain the temperature standard deviations, a sliding 24-h period of data over 30–50 km in altitude and a longitude range from 45W-70W was divided into five latitude regions. The resulting standard deviations are shown in Figure 6C. The stratospheric temperature standard deviations in the northern hemisphere sectors peak near 12 January and 18 January, and show a minimum in activity near 14 January. These variations are not observed near the equatorial region or south of the equator in the stratosphere. Note that the AIRS satellite observations were not sensitive to the peak in activity on 12 January shown by NAVGEM, which may be due in part to AIRS variance calculations being sensitive to longer vertical wavelength GWs and horizontal GW scales <500 km. In Figure 6D, the same analysis is performed again from 75-95 km and shows clear decreases in temperature standard deviation near 14 January for northern, equatorial, and southern latitudes in this longitudinal sector, implying a link between northern and southern hemispheric dynamics at altitudes in the MLT region. Note that the polar region is not included at these altitudes due to semidiurnal tidal dominance. From 16 January onward, all latitudinal study regions show some daily variability in temperature standard deviation, but no significant decreases in temperature standard deviation over the time period.

These findings imply that mesospheric temperature and meridional winds associated with the QTDW as well as GW activity on a larger scale may be linked to EPB activity. The times of lowest EPB activity in the first half of the observation period overlap with both decreased GW variances in the stratosphere in the northern hemisphere, and decreased temperature standard deviation in the MLT over the equatorial region and southern hemisphere. Additionally, the two nights of no EPB activity on 13 and 15 January correspond to southward meridional winds in the mesosphere associated with a specific phase of the QTDW. During the second half of the observation period from 16–24 January, post sunset EPBs (increased ROTI and observed 630 nm airglow depletions) were observed on every night, with the four strongest nights overlapping northward meridional winds and coldest temperatures in the MLT region.

Strong northward meridional winds associated with the QTDW, which allow for southward GW propagation to higher altitudes in the thermosphere during this time period would have implications for GW-induced perturbations in the thermosphere. Additionally, NAVGEM demonstrated a lower standard deviation of temperature during periods of lower EPB activity, and higher standard deviation of temperature during times of increased activity overlapping the region of the polar vortex (20–60N). Disruptions to the polar vortex in the northern hemisphere have been shown to influence the QTDW amplitude both at lower latitudes (Ma et al., 2017) and in the southern hemisphere (McCormack et al., 2009; Ern et al., 2013). It is also noted in this longitudinal sector (45–70W), the magnetic equator is located southward of the geographic equator, ~10S, placing it well within the region of the QTDW. Thus, this southward position would allow for GW propagation through the QTDW wind field before reaching the thermosphere, potentially providing seed perturbations for EPBs near the geomagnetic equator via GWs generated at lower latitudes in the northern hemisphere. Furthermore, the presence of the QTDW itself, and its structure in the upper-mesospheric and lower thermospheric temperature and winds, may have implications for EPB seeding as well.

4 Discussion

An oscillation was observed in EBPs (ROTI and 630 nm airglow) over the Western region of South America during 10–24 January

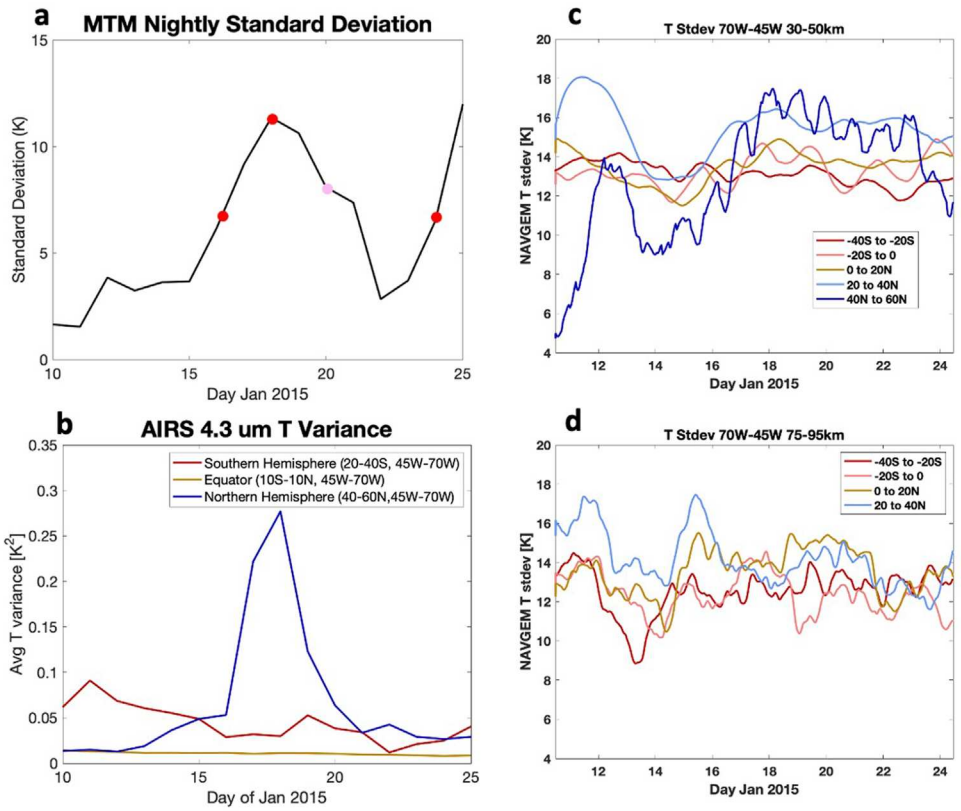

FIGURE 6
Plot **(A)** shows the MTM standard deviation of temperatures. The three nights of largest ROTI values and 630 nm depletions extending below 20S MLAT denoted with red dots, and the fourth largest night of ROTI values is denoted in pink. Plot **(B)** shows AIRS 4.3 μm brightness temperature perturbation variances plotted in the latitude sector from 45W-75W. The data are calculated for regions overlapping the polar vortex in the northern hemisphere (blue line), regions overlapping the equator (gold line), and regions overlapping the ground-based observations in the southern hemisphere (red line). Plot **(C)** shows NAVGEM temperature standard deviation for five latitudinal ranges moving over a 24-h window that includes values from 30 to 50 km in altitude, and 45W–70W in longitude. The stratospheric data indicate a significant dip in wave activity in the northern hemisphere but not in the southern hemisphere near 14 January. Plot **(D)** shows the same as Plot **(C)** but for altitudes from 75 to 95 km, and indicates a dip in wave activity near 14 January in the northern and southern hemispheres.

2015. The strongest peaks in the oscillation coincided with the northward meridional wind phase of the QTDW in the mesosphere region near 85 km in altitude. MTM data demonstrated that the strongest peaks in EPB activity inferred from the ROTI values and 630 nm airglow depletions coincided with days where the coldest temperatures were measured near 87 km by the MTM OH T. These peaks also coincided with higher standard deviations of MTM OH T and higher AIRS temperature perturbation variances in the northern hemisphere (40–60N). Additionally, 2 days with no observed EPBs corresponded to lower GW activity in the stratosphere observed by AIRS in the northern hemisphere, lower MTM and NAVGEM simulated temperature standard deviations in the MLT region, and southward winds and higher temperatures associated with the QTDW in the mesosphere. These observations were made over a time period of relatively quiet solar and geomagnetic activity.

While the period of study is 2 weeks, it indicates the possible role that the QTDW and interhemispheric coupling, both in the neutral atmosphere and the ionosphere, may play in the occurrence and intensity of EPBs. It is important to note that multiple factors play a role in the prevalence of EPBs and their generation and seeding mechanisms. The data presented here demonstrate one aspect of neutral atmospheric dynamical correlations with EPBs, which can arise from multiple sources. Further studies are needed to understand longer term trends associated with the QTDW and EPBs.

Data availability statement

Publicly available datasets were analyzed in this study. This data can be found here: Quick-look images and movies of 630 nm airglow observations from El Leoncito Observatory are available from the Boston University. All-Sky Imager network Archives: www.buimaging.com GPS observations are freely available through Centro Sismologico Nacional archive (https://gps.csn.uchile.cl/) Mesospheric Temperature Mapper Data are available on USU Box (password upon request): http://digitalcommons.usu.edu/ail/ NAVGEM output for this time period are cleared for public release and available upon request from stephen.eckermann.civ@us.navy.mil.

Author contributions

KB: Formal Analysis, Investigation, Methodology, Project administration, Supervision, Writing–original draft, Writing–review and editing. KK: Formal Analysis, Investigation, Methodology, Software, Writing–review and editing. PI: Data curation, Formal Analysis, Investigation, Methodology, Software, Writing–review and editing. JN: Formal Analysis, Investigation, Software, Writing–review and editing. SE: Data curation, Software, Writing–review and editing. P-DP: Data curation, Formal Analysis, Writing–review and editing. CM: Data curation, Writing–review and editing. CK: Formal Analysis, Writing–review and editing. SP: Formal Analysis, Writing–review and editing. JS: Funding acquisition, Investigation, Project administration, Writing–review and editing. YZ: Data curation, Writing–review and editing. MZ: Writing–review and editing.

Funding

The author(s) declare that financial support was received for the research, authorship, and/or publication of this article. This research was supported under DARPA Cooperative Agreement HR00112120003 via a subcontract with Embry-Riddle Aeronautical University. This work is approved for public release; distribution is unlimited. The content of the information does not necessarily reflect the position or the policy of the Government, and no official endorsement should be inferred. (KB, JN, CBK, PI, JS, MZ, KK). NRL's research was supported by the DARPA AtmoSense program, and NRL's NAVGEM reanalysis runs were made possible by the DoD High-Performance Computer Modernization Program via grants of computer time at the Navy DoD Supercomputing Resource Center. Additional research by KB, KK, SP, and JN was funded under NSF AGS 1944027 and NASA 80NSSC21K0002. Support for the operations of the USU MTM and associated OH data analyses were proved by NSF AGS 1911970. CM acknowledges the support of NSF Aeronomy grant #2152365. CM thanks the Director and personnel of CASLEO (Complejo Astronomico El Leoncito) for their continuing support of the BU all-sky imager.

Conflict of interest

Author PI was employed by Computational Physics, Inc.

The remaining authors declare that the research was conducted in the absence of any commercial or financial relationships that could be construed as a potential conflict of interest.

Publisher's note

References

Aa, E., Zhang, S.-R., Coster, A. J., Erickson, P. J., and Rideout, W. (2023a). Multi-instrumental analysis of the day-to-day variability of equatorial plasma bubbles. *Front. Astron. Space Sci.* 10, 1167245. doi:10.3389/fspas.2023.1167245

Aa, E., Zhang, S.-R., Liu, G., Eastes, R. W., Wang, W., Karan, D. K., et al. (2023b). Statistical analysis of equatorial plasma bubbles climatology and multi-day periodicity using GOLD observations. *Geophys. Res. Lett.* 50, e2023GL103510. doi:10.1029/2023gl103510

Aa, E., Zou, S., Ridley, A. J., Zhang, S.-R., Coster, A. J., Erickson, P. J., et al. (2019). Merging of storm time midlatitude traveling ionospheric disturbances and equatorial plasma bubbles. *Space weather.* 17, 285–298. doi:10.1029/2018SW002101

Abdu, M. A. (2012). Equatorial spread F/plasma bubble irregularities under storm time disturbance electric fields. *J. Atmos. Sol. Terr. Phys.* 75, 44–56. doi:10.1016/j.jastp.2011.04.024

Adhya, P., and Valladares, C. E. (2023). Magnetic storm effects on the occurrence and characteristics of plasma bubbles. *J. Geophys. Res. Space Phys.* 128, e2023JA031292. doi:10.1029/2023JA031292

Amadi, B. C., Qian, L., de Paula, E. R., MclNerney, J. M., Kherani, E. A., Santos, A. M., et al. (2023). Intensification and weakening of equatorial plasma bubble development observed by GOLD during different phases of a geomagnetic storm. *J. Geophys. Res. Space Phys.* 128, e2022JA031262. doi:10.1029/2022JA031262

Bhattacharyya, A. (2022). Equatorial plasma bubbles: a review. *Atmosphere* 13 (10), 1637. doi:10.3390/atmos13101637

Burks, D., and Leovy, C. (1986). Planetary waves near the mesospheric easterly jet. *Geophys. Res. Lett.* 13 (3), 193–196. doi:10.1029/gl013i003p00193

Carmo, C. S., Dai, L., Denardini, C. M., Figueiredo, CAOB, Wrasse, C. M., Resende, L. C. A., et al. (2023). Equatorial plasma bubbles features over the Brazilian sector according to the solar cycle and geomagnetic activity level. *Front. Astron. Space Sci.* 10, 1252511. doi:10.3389/fspas.2023.1252511

Chou, M.-Y., Wu, Q., Pedatella, N. M., Cherniak, I., Schreiner, W. S., and Braun, J. (2020). Climatology of the equatorialplasma bubbles captured byFORMOSAT-3/COSMIC. *J. Geophys. Res. Space Phys.* 124. doi:10.1029/2019JA027680

Chou, M.-Y., Yue, J., Sassi, F., McDonald, S., Tate, J., Pedatella, N., et al. (2023). Modeling the day-to-day variability of midnight equatorial plasma bubbles with Sami3/SD-WACCM-X. *J. Geophys. Res. Space Phys.* 128, e2023JA031585. doi:10.1029/2023JA031585

Craig, R., Vincent, R., Fraser, G., and Smith, M. J. (1980). The quasi 2-day wave in the Southern Hemisphere mesosphere. *Nature* 287, 319–320. doi:10.1038/287319a0

de Jesus, R., Batista, I. S., Takahashi, H., de Paula, E. R., Barros, D., Figueiredo, C. A. O. B., et al. (2020). Morphological features of ionospheric scintillations during high solar activity using GPS observations over the South American sector. *J. Geophys. Research:Space Phys.* 124. doi:10.1029/2019JA027441

Eckermann, S. D., Ma, J., Hoppel, K. W., Kuhl, D. D., Allen, D. R., Doyle, J. A., et al. (2018). High-altitude (0-100 km) global atmospheric reanalysis system: description and application to the 2014 austral winter of the Deep Propagating Gravity-Wave Experiment (DEEPWAVE). *Mon. Wea. Rev.* 146, 2639–2666. doi:10.1175/MWR-D-17-0386.1

Ern, M., Preusse, P., Kalisch, S., Kaufmann, M., and Riese, M. (2013). Role of gravity waves in the forcing of quasi two-day waves in the mesosphere: an observational study. *J. Geophys. Res. Atmos.* 118, 3467–3485. doi:10.1029/2012JD018208

Forbes, J. M., Heelis, R., Zhang, X., Englert, C. R., Harding, B. J., He, M., et al. (2021). Q2DW-tide and -ionosphere interactions as observed from ICON and ground-based radars. *J. Geophys. Res. Space Phys.* 126, e2021JA029961. doi:10.1029/2021JA029961

Fritts, D. C., Vadas, S. L., Riggin, D. M., Abdu, M. A., Batista, I. S., Takahashi, H., et al. (2008). Gravity wave and tidal influences on equatorial spread F based on observations during the Spread F Experiment (SpreadFEx). *Ann. Geophys.* 26, 3235–3252. doi:10.5194/angeo-26-3235-2008

Gjerloev, J. W. (2012). The SuperMAG data processing technique. *J. Geophys. Res.* 117 (A9), A09213. doi:10.1029/2012JA017683

Haase, J. S., Dautermann, T., Taylor, M. J., Chapagain, N., Calais, E., and Pautet, D. (2010). Propagation of plasma bubbles observed in Brazil from GPS and airglow data. *Adv. Space Res.* 47, 1758–1776. doi:10.1016/j.asr.2010.09.025

He, M., Chau, J. L., Forbes, J. M., Zhang, X., Englert, C. R., Harding, B. J., et al. (2021). Quasi-2-day wave in low-latitude atmospheric winds as viewed from the

ground and space during January–March, 2020. *Geophys. Res. Lett.* 48, e2021GL093466. doi:10.1029/2021GL093466

Hecht, J. H., Walterscheid, R. L., Gelinas, L. J., Vincent, R. A., Reid, I. M., and Woithe, J. M. (2010). Observations of the phase-locked 2 day wave over the Australian sector using medium-frequency radar and airglow data. *J. Geophys. Res.* 115, D16115. doi:10.1029/2009JD013772

Hickey, D. A., and Martinis, C. (2018). All-sky imaging observations of the interaction between the brightness wave and ESF airglow depletions. *JGR Space Phys.* 125. doi:10.1029/2019JA027232

Hoffmann, L., and Alexander, M. J. (2009). Retrieval of stratospheric temperatures from Atmospheric Infrared Sounder radiance measurements for gravity wave studies. *J. Geophys. Res.* 114, D07105. doi:10.1029/2008JD011241

Huang, C. S. (2018). Effects of the postsunset vertical plasma drift on the generation of equatorial spread F. *Prog. Earth Planet Sci.* 5, 3. doi:10.1186/s40645-017-0155-4

Huang, C. -S., and Hairston, M. R. (2015). The postsunset vertical plasma drift and its effects on the generation of equatorial plasma bubbles observed by the C/NOFS satellite. *J. Geophys. Res. Space Physics* 120, 2263–2275. doi:10.1002/2014JA020735

Huba, J. D. (2022). Generalized Rayleigh-Taylor instability: ion inertia, acceleration forces, and *E* region drivers. *JGR. Space Phys.* 127, e2022JA030474. doi:10.1029/2022JA030474

Huba, J. D., Hellis, R., and Maute, A. (2021). Large-scale O+ depletions observed by ICON in the post-midnight topside ionosphere: data/model comparison. *Geophys. Res. Lett.* 48, e2020GL0920061. doi:10.1029/2020gl092061

Huba, J. D., and Krall, J. (2013). Impact of meridional winds on equatorial spread F: revisited. *Geophys. Res. Lett.* 40 (7), 1268–1272. doi:10.1002/grl.50292

Hudson, M. K., and Kennel, C. F. (1975). Linear theory of equatorial spread F. *J. Geophys. Res.* 80, 4581–4590. doi:10.1029/ja080i034p04581

Hysell, D. L. (2000). An overview and synthesis of plasma irregularities in equatorial spread-F. *J. Atmos. Solar-Terr. Phys.* 62, 1037–1056. doi:10.1016/S1364-6826(00)00095-X

Hysell, D. L., and Burcham, J. D. (1998). JULIA radar studies of equatorial spread F. *J. Geophys. Res.* 103, 29155–29167. doi:10.1029/98ja02655

Iimura, H., Fritts, D. C., Lieberman, R. S., Janches, D., Mitchell, N. J., Franke, S. J., et al. (2021). Climatology of quasi-2-day wave structure and variability at middle latitudes in the northern and southern hemispheres. *J. Atmos. Solar-Terrestrial Phys.* 221, 105690. doi:10.1016/j.jastp.2021.105690

Inchin, P. A., Bhatt, A., Cummer, S. A., Eckermann, S. D., Harding, B. J., Kuhl, D. D., et al. (2023). Multi-Layer evolution of acoustic-gravity waves and ionospheric disturbances over the United States after the 2022 hunga Tonga volcano eruption. *AGU Adv.* 4. doi:10.1029/2023AV000870

Jacobi, C. K. F., and Pogoreltsev, A. (2006). Quasi two-day-wave modulation of gravity wave flux and consequences for the planetary wave propagation in a simple circulation model. *J. Atmos. Solar-Terrestrial Phys.* 68, 283–292. doi:10.1016/j.jastp.2005.01.017

Karan, D. K., Daniell, R. E., England, S. L., Martinis, C. R., Eastes, R. W., Burns, A. G., et al. (2020). First zonal drift velocity measurement of equatorial plasma bubbles (EPBs) from a geostationary orbit using GOLD data. *J. Geophys. Res. Space Phys.* 125, e2020JA028173. doi:10.1029/2020JA028173

Karan, D. K., Eastes, R. W., Daniell, R. E., Martinis, C. R., and McClintock, W. E. (2023). GOLD mission's observation about the geomagnetic storm effects on the nighttime equatorial ionization anomaly (EIA) and equatorial plasma bubbles (EPB) during a solar minimum equinox. *Space weather.* 21, e2022SW003321. doi:10.1029/2022SW003321

Kepkar, A., Arras, C., Wickert, J., Schuh, H., Alizadeh, M., and Tsai, L.-C. (2020). Occurrence climatology of equatorial plasma bubbles derived using FormoSat-3/COSMIC GPS radio occultation data. *Ann. Geophys.* 38, 611–623. doi:10.5194/angeo-38-611-2020

Lay, E. H. (2018). Ionospheric irregularities and acoustic/gravity wave activity above low-latitude thunderstorms. *Geophys. Res. Lett.* 45, 90–97. doi:10.1002/2017GL076058

Lieberman, R. S., Riggin, D. M., Nguyen, V., Palo, S. E., Siskind, D. E., Mitchell, N. J., et al. (2017). Global observations of 2 day wave coupling to the diurnal tide in a high-altitude forecast-assimilation system. *J. Geophys. Res. Atmos.* 122, 4135–4149. doi:10.1002/2016JD025144

Ma, Z., Gong, Y., Zhang, S., Zhao, Q., Huang, C., Huang, K., et al. (2017). Responses of quasi 2 Day waves in the MLT region to the 2013 SSW revealed by a meteor radar chain. *Geophys. Res. Lett.* 44, 9142–9150. doi:10.1002/2017GL074597

Martinis, C., Baumgardner, J., Mendillo, M., Su, S.-Y., and Aponte, N. (2009). Brightening of 630.0 nm equatorial spread-Fairglow depletions. *J. Geophys. Res.* 114, A06318. doi:10.1029/2008JA013931

Martinis, C., Baumgardner, J., Wroten, J., and Mendillo, M. (2018). All-sky-imaging capabilities for ionospheric space weather research using geomagnetic conjugate point observing sites. *Adv. Space Res.* 61, 1636–1651. doi:10.1016/j.asr.2017.07.021

Martinis, C., Mendillo, M. J., and Aarons, J. (2005). Toward a synthesis of equatorial spread F onset and suppression during geomagnetic storms. *J. Geophys. Res. Space. Phys.* 110. doi:10.1029/2003JA010362

McCormack, J. P., Coy, L., and Hoppel, K. W. (2009). Evolution of the quasi 2-day wave during January 2006. *J. Geophys. Res.* 114, D20115. doi:10.1029/2009JD012239

Newell, P. T., and Gjerloev, J. W. (2011a). Evaluation of SuperMAG auroral electrojet indices as indicators of substorms and auroral power. *J. Geophys. Res.* 116 (A12), A12211. doi:10.1029/2011JA016779

Newell, P. T., and Gjerloev, J. W. (2011b). Substorm and magnetosphere characteristic scales inferred from the SuperMAG auroral electrojet indices. *J. Geophys. Res.* 116 (A12), 12232. doi:10.1029/2011JA016936

Otsuka, Y. (2018). Review of the generation mechanisms of post-midnight irregularities in the equatorial and low-latitude ionosphere. *Prog. Earth Planet Sci.* 5, 57. doi:10.1186/s40645-018-0212-7

Pancheva, D., Mukhtarov, P., and Siskind, D. E. (2018). Climatology of the quasi-2-day waves observed in the MLS/Aura measurements (2005–2014). *J. Atmos. Solar-Terrestrial Phys.* 171, 210–224. doi:10.1016/j.jastp.2017.05.002

Pancheva, D. V., Mukhtarov, P. J., Shepherd, M. G., Mitchell, N. J., Fritts, D. C., Riggin, D. M., et al. (2006). Two-day wave coupling of the low-latitude atmosphere-ionosphere system. *J. Geophys. Res.* 111, A07313. doi:10.1029/2005JA011562

Panda, D., Senapati, B., Tyagi, B., and Kundu, B. (2019). Effects of Rayleigh-Taylor instability and ionospheric plasma bubbles on the global navigation satellite System signal. *J. Asian Earth Sci.* 170, 225–233. doi:10.1016/j.jseaes.2018.11.006

Park, J., Mende, S. B., Eastes, R. W., and Frey, H. U. (2022). Climatology of equatorial plasma bubbles in ionospheric connection explorer/far-UltraViolet (ICON/FUV) limb images. *J. Astron. Space Sci.* 39 (3), 87–98. doi:10.5140/JASS.2022.39.3.87

Pautet, P.-D., Taylor, M. J., Chapagain, N. P., Takahashi, H., Medeiros, A. F., Sao Sabbas, F. T., et al. (2009). Simultaneous observations of equatorial F-region plasma depletions over Brazil during the Spread-F Experiment (SpreadFEx). *Ann. Geophys.* 27, 2371–2381. doi:10.5194/angeo-27-2371-2009

Pendleton, W. R., Jr., Taylor, M. J., and Gardner, L. C. (2000). Terdiurnal oscillations in OH Meinel rotational temperatures for fall conditions at northern mid-latitude sites. *Geophys. Res. Lett.* 27 (12), 1799–1802. doi:10.1029/2000gl003744

Pi, X., Mannucci, A. J., Lundqwister, U. J., and Ho, C. M. (1997). Monitoring of global ionospheric irregularities using the worldwide GPS Network. *Geophys. Res. Lett.* 24, 2283–2286. doi:10.1029/97GL02273

PugmireJonathan Rich (2018). Mesospheric gravity wave climatology and variances over the Andes mountains. *All Graduate Theses Diss. Spring 1920 Summer*, 7387. doi:10.26076/4a0e-3308

Rajesh, P. K., Lin, C. C. H., Lin, J. T., Lin, C. Y., Liu, J. Y., Matsuo, T., et al. (2022). Extreme poleward expanding super plasma bubbles over Asia-Pacific region triggered by Tonga volcano eruption during the recovery-phase of geomagnetic storm. *Geophys. Res. Lett.* 49, e2022GL099798. doi:10.1029/2022GL099798

Saha, S., Pallamraju, D., and Ghodpage, R. N. (2022). Investigations of equatorial plasma bubbles as observed in the OI 630 nm nightglow emissions over off-equatorial and low-latitudinal locations over Indian longitudes. *Adv. Space Res* 70, 3686–3698. doi:10.1016/j.asr.2022.08.023

Singh, D., Mitra, G., Guharay, A., Pallamraju, D., and Gurubaran, S. (2024). Quasi-two-day wave amplification through interhemispheric coupling during the 2010 austral summer. *Adv. Space Res.* 73 (7), 3452–3463. doi:10.1016/j.asr.2023.06.044

Singh, S., Johnson, F. S., and Power, R. A. (1997). Gravity wave seeding of equatorial plasma bubbles. *J. Geophys. Res.* 102 (A4), 7399–7410. doi:10.1029/96ja03998

Sori, T., Shinbori, A., Otsuka, Y., Tsugawa, T., and Nishioka, M. (2021). The occurrence feature of plasma bubbles in the equatorial to midlatitude ionosphere during geomagnetic storms using long-term GNSS-TEC data. *J. Geophys. Res. Space Phys.* 126, e2020JA029010. doi:10.1029/2020ja029010

Sousasantos, J., Gomez Socola, J., Rodrigues, F. S., Eastes, R. W., Brum, C. G. M., and Terra, P. (2023). Severe L-band scintillation over low-to-mid latitudes caused by an extreme equatorial plasma bubble: joint observations from ground-based monitors and GOLD. *Earth, Planets Space* 75, 41–1. doi:10.1186/s40623-023-01797-5

Stolle, C., Luhr, H., Rother, M., and Balasis, G. (2006). Magnetic signatures of equatorial spread F as observed by the CHAMP satellite. *J. Geophys. Res.* 111, A02304. doi:10.1029/2005JA011184

Sultan, P. J. (1996). Linear theory and modeling of the Rayleigh-Taylor instability leading to the occurrence of equatorial spread F. *J. Geophys. Res. Space Phys.* 101, 26875–26891. doi:10.1029/96JA00682

Takahashi, H., Taylor, M. J., Pautet, P.-D., Medeiros, A. F., Gobbi, D., Wrasse, C. M., et al. (2009). Simultaneous observation of ionospheric plasma bubbles and mesospheric gravity waves during the SpreadFEx Campaign. *Ann. Geophy.* 27 (4), 1477–1487. doi:10.5194/angeo-27-1477-2009

Taori, A., Patra, A. K., and Joshi, L. M. (2011). Gravity wave seeding of equatorial plasma bubbles: an investigation with simultaneous F region, E region, and middle atmospheric measurements. *J. Geophys. Res.* 116, A05310. doi:10.1029/2010JA016229

Taylor, M. J., Gardner, L. C., and Pendleton, W. R., Jr. (2001). Long period wave signatures in mesospheric OH Meinel (6,2) band intensity and rotational temperature at midlatitudes. *Adv. Space Res.* 27 (6 – 7), 1171–1179. doi:10.1016/s0273-1177(01)00153-3

Taylor, M. J., Pendleton, W. R., Jr., Gardner, C. S., and States, R. J. (1999). Comparison of terdiurnal tidal oscillations in mesospheric OH rotational temperature and Na lidar temperature measurements at midlatitudes for fall/spring conditions. *Earth Planets Space* 51, 877–885. doi:10.1186/bf03353246

Walterscheid, R. L., Hecht, J. H., Gelinas, L. J., MacKinnon, A., Vincent, R. A., Reid, I. M., et al. (2015). Simultaneous observations of the phase-locked 2 day wave at adelaide, cerro pachon, and Darwin. *J. Geophys. Res. Atmos.* 120, 1808–1825. doi:10.1002/2014JD022016

Yasui, R., Soto, K., and Miyoshi, Y. (2021). Roles of rossby waves, rossby-gravity waves, and gravity waves generated in the middle atmosphere for interhemispheric coupling. *J. Atmos. Sci.* 78, 3867–3888. doi:10.1175/JAS-D-21-0045.1

Yizengaw, E., Retterer, P. E. E., Roddy, P., Groves, K., Caton, R., Baki, P., et al. (2013). Post-midnight bubbles and scintillations in the quiet-time June solstice. *Geophys Res. Lett.* 40, 5592–5597. doi:10.1002/2013GL058307

Yokoyama, T., Jin, H., Shinagawa, H., and Liu, H. (2019). Seeding of equatorial plasma bubbles by vertical neutral wind. *Geophys. Res. Lett.* 46, 7088–7095. doi:10.1029/2019GL083629

Yue, J., Wang, W., Richmond, A. D., and Liu, H.-L. (2012). Quasi-two-day wave coupling of the mesosphere and lower thermosphere-ionosphere in the TIME-GCM: two-day oscillations in the ionosphere. *J. Geophys. Res.* 117, A07305. doi:10.1029/2012JA017815

Zhao, Y., Taylor, M. J., and Chu, X. (2005). Comparison of simultaneous Na lidar and mesospheric nightglow temperature measurements and the effects of tides on the emission layer heights. *J. Geophys. Res.* 110, D09S07. doi:10.1029/2004JD005115